

Alignment and characterization of the two-stage time delay compensating XUV monochromator

Martin Eckstein,¹ Johan Hummert,¹ Markus Kubin,^{1, a)} Chung-Hsin Yang,^{1, b)} Fabio Frassetto,² Luca Poletto,² Marc J. J. Vrakking,¹ and Oleg Kornilov^{1, c)}

¹⁾ *Max Born Institute, Max-Born-Straße 2A, 12489 Berlin, Germany.*

²⁾ *National Research Council - Institute of Photonics and Nanotechnologies (CNR-IFN), via Trasea 7, I-35131 Padova, Italy.*

We present the design, implementation and alignment procedure for a two-stage time delay compensating monochromator. The setup spectrally filters the radiation of a high-order harmonic generation source providing wavelength-selected XUV pulses with a bandwidth of 300 to 600 meV in the photon energy range of 3 to 50 eV. XUV pulses as short as 12 ± 3 fs are demonstrated. Transmission of the 400 nm (3.1 eV) light facilitates precise alignment of the monochromator. This alignment strategy together with the stable mechanical design of the motorized beamline components enables us to automatically scan the XUV photon energy in pump-probe experiments that require XUV beam pointing stability. The performance of the beamline is demonstrated by the generation of IR-assisted sidebands in XUV photoionization of argon atoms.

I. INTRODUCTION

Ultrafast laser pulses in the extreme-ultraviolet (XUV) range become more and more instrumental in studies of molecules, liquids and solids. Development of novel XUV laser sources such as free electron lasers and high-order harmonic generation (HHG) sources allows experiments with femtosecond and even attosecond time resolution, which are capable of following nuclear and electron dynamics in real time^{1,2}. In many cases ultrafast XUV studies benefit from control of the XUV photon energy. Such control is routinely available for free electron lasers. However, in the HHG process a wide range of XUV energies is inherently generated and spectral filtering is necessary to produce bandwidth-limited pulses that are suitable for experiments with simultaneous time and energy resolution.

Selection of the photon energy from an HHG source requires an XUV monochromator. Some of the simplest monochromators are realized using specially designed multilayer mirrors optimized for reflection in a desired XUV photon energy range³. This solution is convenient when a fixed range of photon energies is needed for the experiment, but changing the photon energy requires replacement of the multilayer mirrors.

More versatile tools are based on diffraction. Such systems have been realized using spherical and toroidal diffraction gratings^{4,5}, plane gratings in normal and off-plane configurations⁶⁻⁸ and Fresnel zone plates⁹⁻¹¹. Designs based on diffraction gratings can provide very high spectral resolution at the expense of temporal resolution. Diffraction on a transmission or reflection grating leads to an optical path difference (OPD) across the spatial

profile of the beam. The path difference is proportional to the number of illuminated grooves N and can be expressed as $OPD = Nm\lambda$, where m is the diffraction order and λ is the wavelength of the light. Correspondingly, there is a delay that accumulates across the beam profile, which stretches the pulse in time and reduces the temporal resolution of a pump-probe experiment.

This problem can be overcome by using a time delay compensating scheme with two diffraction gratings^{12,13}. The pulse stretched by the first diffraction grating is compressed upon reflection from the second identical grating mounted in a mirrored configuration. This optical design has been previously realized by Poletto et al⁶ and demonstrated excellent temporal resolution for a typical HHG source. Here we describe a new implementation of the time delay compensating monochromator (TDCM) beamline employing two diffraction gratings. The optical design of the monochromator is similar to that described earlier⁶ and is also based on off-plane grating mounts. The main design goals of the present setup, making it different from those published earlier, is optimization for a wide range of photon energies (3 to 50 eV), the accomplishment of stable long-term operation (days of unattended operation) and reliability in automated switching between photon energies in the course of experiments.

The next section describes the optical design of the monochromator and lists parameters of the optical elements used. The third section presents the mechanical implementation and alignment procedures necessary for stable and reliable operation. Section IV is devoted to energy, transmission and pulse duration characterization of the monochromator setup. In the last section application of the setup for the generation of IR-assisted sideband structures^{14,15} in XUV photoionization of argon atoms is discussed.

^{a)} present address: Helmholtz-Zentrum Berlin, Albert-Einstein-Strae 15, 12489 Berlin, Germany.

^{b)} present address: Academia Sinica, 128 Academia Road, Section 2, Nankang, Taipei 115, Taiwan.

^{c)} Electronic mail: kornilov@mbi-berlin.de

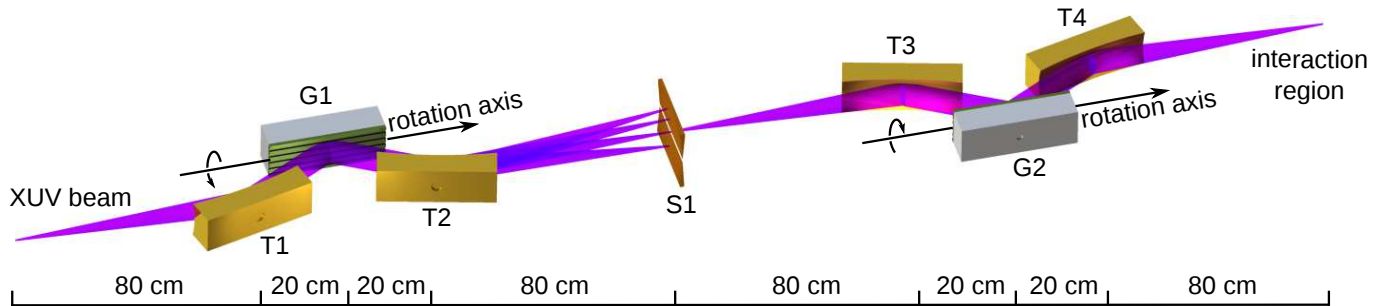


FIG. 1. Optical layout of the TDCM, consisting of four toroidal mirrors (T1-T4), two diffraction gratings (G1, G2) operated in the off-plane mount and the monochromator slit (S1). The length scale is shown at the bottom. The XUV beam is spectrally dispersed by the first stage (T1+G1+T2) and is filtered by the slit (S1). At this point the beam is stretched in time. The second stage (T3+G2+T4) recompresses the XUV pulse and guides the beam towards the interaction region of an experimental endstation.

II. OPTICAL DESIGN

A brief description of the monochromator beamline has recently been published elsewhere². The full optical layout of the two-grating time delay compensating monochromator (TDCM) is shown in Fig. 1. It consists of four toroidal mirrors, two diffraction gratings and an exchangeable slit. All mirrors have the same focal length of 80 cm and therefore each pair of toroidal mirrors together with the grating between them (T1+G1+T2 and T3+G2+T4) forms a Rowland circle configuration, which minimizes geometric aberrations in beam imaging.

The first toroidal mirror T1 collimates the XUV beam coming from an HHG source and reflects it towards the first grating G1. The desired photon energy is selected by rotating the grating G1 around the so-called conical axis that runs parallel to the grooves of the grating (see also Fig. 2 and the explanation of this figure in the text). The diffracted XUV beam is sent through slit S1 mounted in the focal plane of the second toroidal mirror T2. The pair of toroidal mirrors T3+T4 produces an image of the XUV beam selected by the slit in the interaction region of the endstation that is connected to the monochromator beamline. The second grating G2 is rotated by the same angle as grating G1 and compensates for the temporal stretching induced by the first grating. In our implementation the grating pairs can be exchanged in place to optimize diffraction efficiency. Three grating sets are used with the blaze angles of each pair optimized for a different photon energy range. The parameters of the three grating sets and of the toroidal mirrors are listed in Table I.

The transmission efficiency is an important factor for the design of the two-grating monochromator, because diffraction and reflection efficiencies in the XUV photon energy range are generally low even at grazing incidence. To overcome this difficulty the diffraction gratings in the present layout are used in an off-plane (also called conical diffraction) mount. The ray geometry for the off-plane grating mount is shown in Fig. 2. The grating is mounted with its grooves parallel to the long side of the grating

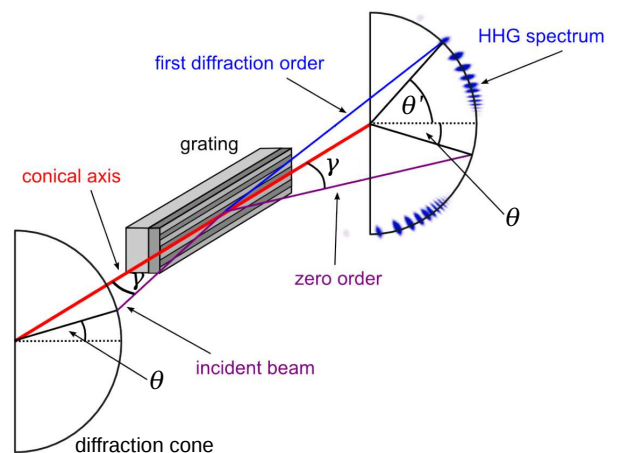


FIG. 2. Off-plane diffraction mount. The XUV beam is incident on the grating mounted with its grooves parallel to the long side of the grating. The diffracted beams are located on a cone with the opening half-angle of γ , which is defined as shown in the figure. The angles of the incident beam θ and the diffracted beam θ' for the given wavelength λ are connected by Eq. (1).

substrate, i.e. perpendicular to the traditional (in-plane) diffraction configuration. The resolving power in this case is smaller than in the traditional configuration using the same grating and beam size, because less grooves are illuminated at the grazing incidence. For this reason the off-plane mount is rarely used in situations, where bright sources are available and efficiency can be sacrificed in favor of spectral resolution. However in femtosecond time-resolved experiments the spectral bandwidth required to support short pulses puts an upper limit on the energy resolution that can be demanded in experiments, while the low yield of HHG sources makes diffraction efficiency a more limiting factor. Here the off-plane mount offers the advantage of very high reflectivity compared to the traditional in-plane grating mount. It was shown that for a blazed grating in the off-plane mount the diffraction ef-

iciency in the direction corresponding to the blaze angle may reach the limit given by the reflectivity of the coating (an Al coating in this case)^{16–19}.

TABLE I. Parameters of the optical elements of the TDCM.

	Toroidal	Grating I	Grating II	Grating III
focal length, cm	80	-	-	-
density, gr/mm	-	150	300	600
blaze angle	-	3.4°	4.3°	7.0°
incident angle	4°	5°	5°	5°
energy range, eV	3-50	14-30	20-38	32-50
peak energy, eV	-	18	28	35
length, mm	90	70	70	70
height, mm	15	15	15	15

In the off-plane geometry, diffraction of a ray incident on the grating at a grazing angle γ forms a cone with an opening angle of 2γ . The grating diffraction equation in the off-plane case reads:

$$\sin \gamma (\sin \theta + \sin \theta') = m \lambda \sigma, \quad (1)$$

where θ is the angle between projections of the incident ray and the grating normal on a plane perpendicular to the grooves, θ' is the angle between projections of the diffracted ray and the grating normal on the same plane, m is the diffraction order, λ is the wavelength of the diffracted light and σ is the groove density. In the operation of the monochromator the grating is rotated around an axis parallel to the grooves and lying in the surface plane of the grating in such a way that the diffracted ray corresponding to the wavelength of choice propagates at the same angle as the incident ray (i. e. $\theta' = \theta$). For this particular wavelength the diffraction equation simplifies to

$$2 \sin \gamma \sin \theta = m \lambda \sigma. \quad (2)$$

The angle θ in this equation corresponds to the rotation angle of the diffraction grating, which is used to select the XUV wavelength λ .

Expected performance of the monochromator is estimated by numerical ray-tracing of the optical setup using parameters of the optical elements given in Table I. The source size is estimated to be 60 μm for the XUV generation layout used in the present experiments. The slit width is 100 μm . With these parameters the ray-tracing calculation delivers estimates of the FWHM bandwidth of the XUV light passing through the slit for a given XUV photon energy and the optical path differences before and after the compensation in the second stage of the monochromator. For the three gratings listed in Table I the spectral resolution in their corresponding energy ranges varies smoothly from 0.15 to 0.5 eV. The optical path difference after the first stage is approximately 100 fs for all gratings and is reduced to 2-4 fs by the compensation in the second stage.

III. MECHANICAL DESIGN AND ALIGNMENT

In experiments with XUV light, the XUV source, the optical elements and the experimental target are located in a vacuum environment, which requires special care when constructing the optical mounts. Additionally, we choose to guide a second laser beam used for pump-probe experiments also in vacuum in close proximity to the XUV beam path to ensure long-term stability of the setup. All this puts stringent constraints on the geometry of the individual optical elements, the mechanical design and the alignment strategy of the TDCM. The most important elements in our implementation of the monochromator are the grating holders. In experiments, the incidence angles on both gratings are tuned precisely to select the ray with the desired photon energy in the first stage, to compensate the induced stretch in the second stage and to maintain the alignment of the ray with respect to the interaction region of the experimental end-station. Therefore stability of the grating holders, their alignment and reproducibility of rotation have a major impact on the overall performance of the TDCM, in particular, on keeping the position of the XUV focus fixed while scanning the XUV photon energy. This section describes the implementation and alignment of the optical elements in our setup. The first subsection describes the design and pre-alignment of the grating holders. The complete beamline is described in the second subsection. The third and fourth subsections provide descriptions of the alignment of the main XUV arm and the second IR arm required for femtosecond pump-probe experiments.

Design and pre-alignment of the grating holders

The correct operation of the monochromator requires that the XUV beam always follows the same optical path in the monochromator independent of the photon energy selected by the gratings. The path should also remain the same when switching between gratings with different groove densities. If the pointing of the XUV beam changed, it would lead to a displacement of the XUV beam in the interaction region and loss of the spatial overlap of the laser beams in the pump-probe experiment. Moreover, substantial changes in pointing of the XUV beam may cause aberrations in the imaging by the toroidal mirrors or lead to stretching of the pulse in the time domain. Parallel displacement of the XUV beam from the optical axis, on the contrary, is not very crucial as long as the geometrical aberrations for the off-axis rays remain small.

For the pointing of the XUV beam to remain constant for all wavelengths the rotation axis must coincide with the axis of the diffraction cone for the selected grating (see Fig. 2). If this is the case, then rotation of the grating moves diffracted rays on this cone. Consequently for every ray(wavelength) there is a rotation angle θ , which sends that ray along the optical path of the monochroma-

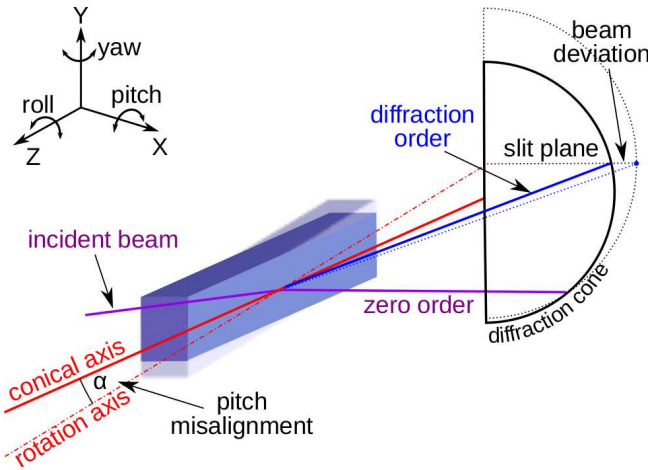


FIG. 3. Misalignment of the grating pitch. The conical axis of the grating is tilted with respect to the rotation axis by an angle α . The new diffraction cone (solid line) has a different axis and a different opening angle as compared to the diffraction cone of the properly aligned grating (dotted line). The misalignment leads to a deviation of the diffracted beam with respect to the optical path of the TDCM (dotted line).

tor (the beam path all elements are aligned to). On the other hand, if the rotation axis is misaligned with respect to the axis of the diffraction cone, the rotation changes the axis and the opening angle of the diffraction cone. This leads to a wavelength-dependent deviation of the diffracted beam from the optical path of the monochromator, i.e. the XUV beam pointing depends on the chosen wavelength. This effect is sketched in Fig. 3 for the case of a misalignment of the grating pitch. Similar effect is observed for a misalignment of the yaw.

It follows that the degrees of freedom provided by the grating holder should be used to align the grating grooves along the rotation axis of the grating holder. The displacement along the grating normal (X in Fig. 2) in this case controls the position of the grating surface with respect to the rotation axis and the pitch and yaw angles control the angle between the grating grooves and the rotation axis. We can show that for small grating rotation angles θ the grating pitch is the most critical parameter, while effects of a misalignment in the yaw are an order of magnitude smaller. For a pitch misalignment (shown in Fig. 3) the change in the opening angle of the diffraction cone upon rotation of the grating can be calculated using the following expression:

$$\frac{\cos \gamma'' - \cos \gamma'}{\sin \gamma'' + \sin \gamma'} = \tan \alpha \sin \theta, \quad (3)$$

where α is the pitch misalignment angle between the conical axis and the rotation axis, θ is the grating roll and γ', γ'' are half-angles of the diffraction cone before and after grating rotation, respectively. In the small angle approximation this expression simplifies to

$$\gamma' - \gamma'' = 2\alpha\theta. \quad (4)$$

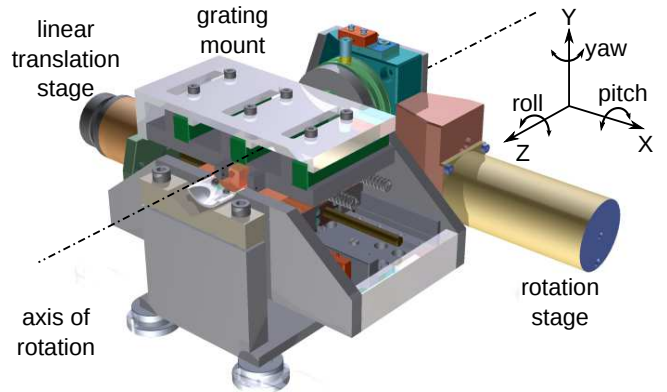


FIG. 4. Assembly drawing of the grating holder. The grating mount housing three gratings with different groove densities is attached to a linear translation stage, which allows exchange of the gratings. The linear stage is mounted on a rotation stage controlling the grating roll angle and thus the selected XUV photon energy. The coordinate system used in the text is defined in the upper right corner of the plot.

Typical spot sizes of the XUV and IR beams in pump-probe experiments are $100 \mu\text{m}$ and therefore the displacements of the XUV beam in the focus have to be limited to $10\text{-}20 \mu\text{m}$. This is equivalent to XUV pointing deviations of less than $25 \mu\text{rad}$. According to the equation above, for a diffraction angle $\theta = 100 \text{ mrad}$ the pitch misalignment angle α should be less than $125 \mu\text{rad}$.

Precise alignment of the pitch and yaw angles and the position in the direction X (for all six gratings in the two stages of the TDCM) are thus required for correct operation over the full wavelength range. Each holder houses three gratings and therefore should in principle provide tunability for $3 \times 3 = 9$ degrees of freedom. To reduce the mechanical complexity of the holders and ease the alignment, we decided to mount the three gratings of each monochromator stage in one common fixed mount, which is precisely machined to ensure that the grating surfaces and their grooves are parallel to each other. The design of the grating holder is shown in Fig. 4. The gratings are exchanged by linearly translating the mount by means of a vacuum-compatible linear translation stage (Micos, model LS-65 UHV). The rotations of the grating are performed by a vacuum-compatible rotation stage (Micos, model DT-65N UHV), which holds the linear stage that carries the gratings. The parallelism of the gratings is checked by examining the reflection of an alignment laser (HeNe laser) from each of the three gratings. The roll angle (see Fig. 4) showed slight deviations, which could be corrected by calibration of the rotation stage.

The holders with fixed grating mounts reduce the number of required degrees of freedom to four: the displacement in the X direction and the roll, pitch and yaw angles for all gratings simultaneously. The roll angle is motorized and is used to tune the monochromator to the desired wavelength. Therefore it does not need alignment, but instead requires wavelength calibration.

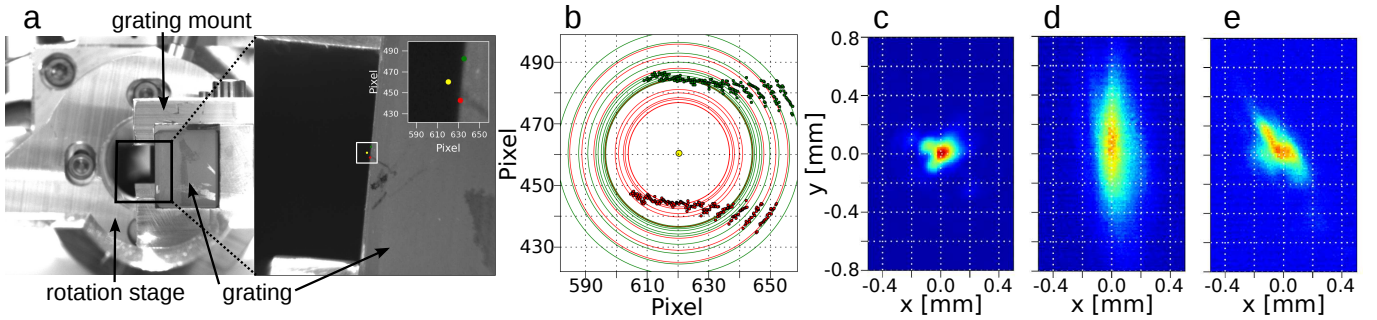


FIG. 5. Alignment of the grating holder. a) High-resolution close-up images of the grating edge with two distinct points (red and green) marked. b) Trajectories followed by two points marked in a), when the grating is rotated around the roll axis and/or displaced along the direction X. The concentric circles fitted to the trajectories help to establish the position of the rotation axis (yellow point). Alignment using the 400 nm light. c) The profile of the 400 nm beam for the grating turned to zero order. The image distortions are caused by diffraction on grating edges. d) The beam stretched by diffraction from the first grating. The beam is centered at zero indicating correct alignment of the grooves (see text). e) The beam stretched by the first grating and recompressed by the second grating.

Alignment of the grating displacement along X and of the grating yaw is performed by imaging the edge of the grating by a CCD camera through a zoom lens with a large magnification, as shown in Fig. 5a. The focal plane of the camera is approximately perpendicular to the rotation axis of the holder and therefore the edge remains in focus when the grating is rotated. For a set of linear stage positions (X) and grating rotation angles θ positions of two recognizable marks on the grating edge (small scratches, labeled by red and green dots in Fig. 5a) are traced. When the grating is rotated, these marks follow circular trajectories shown in Fig. 5b for several linear stage positions. The common center of these circles corresponds to the position of the rotation axis in the focal plane of the CCD camera. The position of the rotation axis is thus extracted with a precision of $5 \mu\text{m}$, estimated by repeating the measurement several times for slightly different CCD camera alignments. This procedure is performed for both edges of the same grating and gives the optimal linear stage position X for each edge. The difference of these optimal positions is used to calculate the residual yaw of the grating, which is then corrected by tilting the grating mount. The estimated precision of $5 \mu\text{m}$ corresponds to an angular precision of $70 \mu\text{rad}$, which is less than the limiting misalignment angle given above.

As mentioned above, the most crucial alignment parameter is the pitch. The high groove densities of the gratings prevent use of optical imaging methods for groove alignment. To overcome this difficulty the grating holders are designed to reach rotation angles of more than 25° , which is sufficient to observe the first order diffraction of a 400 nm beam from the grating with the lowest groove density of 150 grooves per mm. Therefore a 400 nm beam, which is easy to generate with a femtosecond laser, can be used to align the grating pitch with the required precision of less than $125 \mu\text{rad}$.

In this alignment procedure the 400 nm beam is first

reflected from the grating rotated to the zero order. The position of the beam is recorded on a high-resolution beam profiler. The grating is then rotated to the angle corresponding to the first order diffraction of the 400 nm beam ($\theta = 20.1^\circ$). The horizontal displacement of the diffracted beam from the position of the zero-order beam is due to the pitch misalignment of the grating and therefore can be used to adjust the grating.

The 400 nm beam profiles recorded in this alignment procedure are shown in Fig. 5c and d. As required, the beams are located precisely at the same spot on the beam profiler, but the diffracted beam (Fig. 5d) is visibly elongated due to spectral dispersion on the first grating. The alignment procedure is repeated for the second grating holder. Fig. 5e shows the beam profile after installing both grating holders in the 400 nm beam path and rotating both gratings to the first diffraction order. The beam is again positioned precisely at zero and is vertically confined, because the second grating compensates the spectral dispersion induced by the first grating. The increased distortions of the beam profile are caused by diffraction on edges of both gratings. In the case of the XUV beam these effects are significantly reduced compared to those observed for the 400 nm beam, because of smaller XUV beam size and shorter wavelength. Thus aligned the grating holders can be moved and placed at the respective positions in the XUV monochromator beamline.

Implementation of the monochromator beamline

The complete design of the TDCM beamline is shown in Fig. 6. A commercial state-of-the-art laser system (Aurora, Amplitude Technologies) provides ultrashort pulses with 795 nm central wavelength and durations of 25 fs at 1kHz repetition rate. A beam with a pulse energy of about 1 mJ is focused in a gas cell filled with a noble

gas (typically argon) to produce the XUV light via high-order harmonic generation (HHG)²⁰. The XUV beam propagates towards the first section of the monochromator (section A), where the residual IR beam is blocked by a 100 nm thick Al filter (Lebow), which is transparent for XUV photons in the range of 20 to 72 eV. The filter helps to reduce the scattered IR light and protects the first toroidal mirror T1 from Al deposits, which propagate along the laser beam from the HHG cell. The filtered XUV beam is collimated by the first toroidal mirror (T1) positioned 80 cm away from the focus in the HHG cell. The collimated beam impinges on the first diffraction grating G1 at an angle of 5° and is then refocused in the plane of the monochromator slit (S1) by the second toroidal mirror (T2).

In the focal plane the rays diffracted from the grating G1 are located on a cone as shown in Fig. 2. A horizontal slit positioned perpendicular to the cone selects the ray corresponding to the desired photon energy while blocking all other rays. The energy resolution of the monochromator can be adjusted by selecting one of the four slits with fixed widths (50, 100, 200 and 650 μm) mounted on a motorized manipulator. The expected photon energy resolution for the 100 μm slit ranges from 0.15 to 0.5 eV according to ray-tracing estimates given above. This value increases approximately linear with width for wider slits, but only marginal improvement is expected for the 50 μm slit, because of geometrical aberrations induced by toroidal mirrors.

The XUV beam passing through the slit is collimated by the third toroidal mirror (T3) and impinges on the second grating G2. The grating G2 is always rotated by the same angle as grating G1 but in the opposite sense of rotation. This ensures that the temporal stretch induced by diffraction on the first grating is compensated by the second grating. The beam diffracted from G2 is focused by the last toroidal mirror T4 into the interaction region. On its way the beam passes through a hole drilled at 45° in a 2-inch recombination mirror (RM).

There are two auxiliary tools for characterization of the XUV beam, which are implemented in our setup. As can be seen in Fig. 6 the linear translation stage of the grating holder in section A can be used to displace the grating from the path of the XUV beam, which allows the beam to reach the entrance slit of a compact XUV spectrometer (XSPEC)²¹. The spectrometer is used to monitor the full HHG spectrum at the entrance of the monochromator. Similarly, in section B, the XUV beam passing by the grating G2 can reach a calibrated XUV photodiode (AXUV-100, International Radiation Detectors), which is used to monitor the absolute XUV pulse energy passing through the slit of the monochromator. The measured value should be corrected for the diffraction efficiency of grating G2 and the reflectivity of the last toroidal mirror T4 to obtain the XUV pulse energy at the interaction region.

In the present experiments a velocity map imaging spectrometer (VMI)²² is connected at the end of the

monochromator beamline and used for characterization of the beamline, as well as execution of first experiments². The VMI spectrometer can record kinetic energy and angular distributions of both electrons and ions resulting from photoionization by XUV pulses. The target in the present case is a gas jet originating from a 10 μm orifice in the repeller plate of the spectrometer²³.

Alignment

Initial alignment of the TDCM components at their design positions is performed using a HeNe alignment laser. A calibrated 100 μm pinhole is placed at the position of the HHG cell to define the source size. The beam is imaged by a beam profiler after each optical element to ensure proper alignment. Toroidal mirrors are mounted in five-axis vacuum-compatible mirror holders (Alca) and their positions are tuned to minimize imaging aberrations as observed on the beam profiler. The pre-aligned grating holders are placed in their positions ensuring that the incidence angles are equal to the design value of 5°.

Operation of the TDCM requires not only careful alignment of all optical components, but also precise alignment of the driving femtosecond IR beam (and thus the XUV beam) to the optical axis of the setup. This operation should be performed daily and without breaking the vacuum. For this purpose we employ two irises, labeled I1 and I2 in Fig. 6, which are imaged by CCD cameras via vacuum viewports. The first iris is positioned at the entrance to section A of the monochromator before the first toroidal mirror T1. The position of the second iris I2 is chosen such as to increase the precision of alignment. For this a simple 2D ray tracing is performed with the toroidal mirrors replaced by ideal lenses and the gratings removed for simplicity. The results are shown in the inset of Fig. 6. The rays start at the position of the first iris I1 assuming perfect alignment at that iris and follow slightly diverging paths. The second iris I2 is positioned in front of mirror T3, where the spread of the rays is largest, thus maximizing the sensitivity to the deviations from the optical axis. This procedure ensures alignment of the XUV beam with a precision better than 80 μrad , sufficient for correct operation of the TDCM.

The IR/vis/UV arm for the pump-probe experiments

The main purpose of the present TDCM setup is investigation of femtosecond molecular dynamics using pump-probe spectroscopy with XUV pulses. For this purpose a second laser arm is constructed, which is designed to transmit laser pulses in the near-IR, visible or UV ranges. For stability and laser safety the beam in this arm is guided through the same vacuum system as the XUV beam, as shown in Fig. 6. The beam enters the vacuum system through a viewport located in the vicinity of the

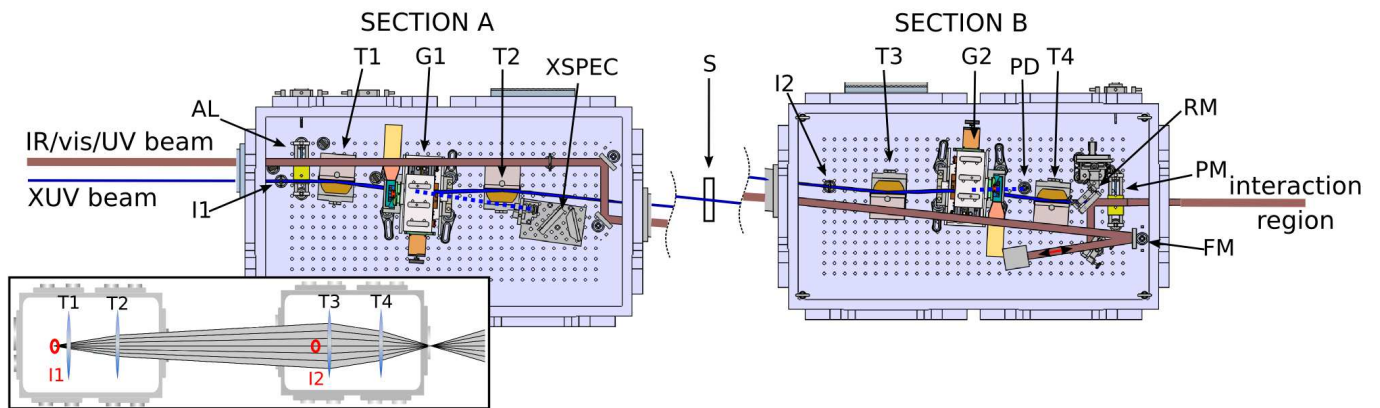


FIG. 6. Schematic drawing of the TDCM beamline: AL - aluminium filter; T1,T2,T3,T4 - toroidal mirrors; G1,G2 - gratings; I1, I2 - XUV alignment irises; S - slit; XSPEC - XUV spectrometer; PD - XUV photodiode; RM - recombination mirror; FM - focusing mirror; PM - pick-off mirror. The inset shows the ray-tracing of the TDCM alignment B used to choose the position of the iris I2 (see text for details).

entrance window of the HHG driving laser. It is guided by two 2-inch mirrors and is incident on a focusing mirror (FM) located at the far end of section B. The converging beam is then recombined with the XUV beam by the recombination mirror RM. For precise control of the focus position, the divergence of the second beam is adjusted by a two-mirror telescope before the beam enters the vacuum system.

To establish the spatial and temporal overlap of the two pulses, a pick-off mirror (PM) can be positioned in the beam after the recombination mirror by means of a manual manipulator. The XUV beam cannot pass through the glass viewport, but when the aluminium filter is moved out of the beam and gratings G1 and G2 are tuned to zero order, the driving IR beam propagates through the monochromator and can be used for pre-alignment of the pump-probe overlap. Fine alignment of the spatial and temporal overlap uses the process of bond softening in H_2^+ molecules²⁴.

IV. CHARACTERIZATION

Three main parameters characterize the performance of the XUV monochromator: the spectral resolution, the temporal resolution and the total transmission of the monochromator beamline. This section describes results of performance tests for these three parameters. All of them depend on the XUV photon energy and therefore the transmission and the spectral resolution of the setup are characterized for several photon energies in the tuning range of the monochromator. The temporal characterization, however, is quite complex and only performed for a photon energy of 29.6 eV, corresponding to the 19th harmonic. These experiments demonstrate the compensation scheme of the TDCM and yield a duration of the XUV pulse of 12 ± 3 fs in good agreement with the previous experiments, which demonstrated the duration of

13 ± 0.5 fs for the 19th harmonic generated at similar experimental conditions²⁵. Further experiments outside of the scope of this work will be performed to test practical limits of the temporal resolution, which are estimated in the Optical design section.

Transmission of the monochromator

The conical diffraction principle used in the present design of the TDCM allows for very high transmission of the XUV radiation even though six optical elements are used in the optical layout. The transmission is further enhanced by using three sets of gratings each optimized for a specific photon energy range. The XUV transmission for the present setup is characterized using two calibrated XUV photodiodes (AXUV-100, International Radiation Detectors). Since both sections of the monochromator are assembled from identical elements, only section B is characterized and the resulting transmission coefficient is squared to obtain transmission of the complete monochromator²⁶.

The first photodiode is mounted on a mechanical manipulator and located after the monochromator slit before the toroidal mirror T3. It measures the total XUV flux entering section B. The second photodiode is mounted after the last toroidal mirror T4 and measures the flux delivered to the interaction region. The measurement is performed for two of the three sets of gratings²⁷ by tuning the gratings from one HHG peak to the other and measuring the incoming and outgoing photon fluxes. The ratio of the two fluxes gives the transmission coefficient for section B. The results of the transmission measurements are shown in Fig. 7. They demonstrate that the transmission is above 3% in the range of the measurement and reaches a value of 15% for the harmonic, which has its diffraction angle close to the blaze angle of the 600 gr/mm grating²⁷.

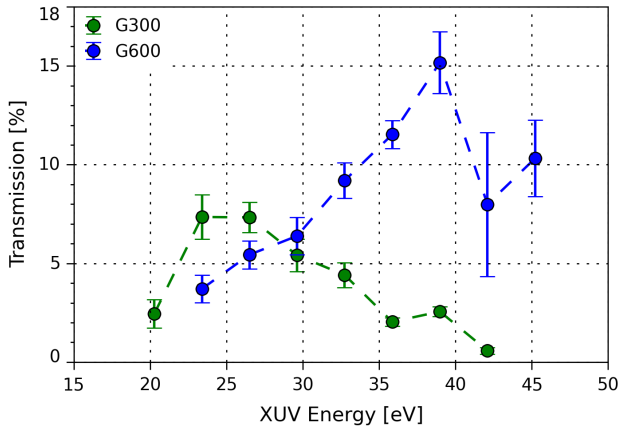


FIG. 7. Transmission coefficients of the full TDCM beamline for the 300 gr/mm (green) and 600 gr/mm (blue) gratings as a function of the XUV photon energy²⁷. The optimal photon energy ranges for the gratings are listed in Table I.

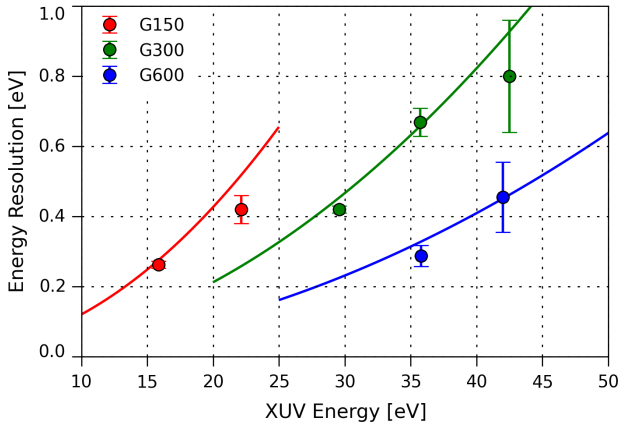


FIG. 8. Energy resolution of the TDCM employing the 100 μm slit. The round symbols correspond to the gratings with groove densities of 150 gr/mm (red), 300 gr/mm (green) and 600 gr/mm (blue). The lines represent estimates of the resolution as described in the text.

Spectral characterization

The spectral resolution of the monochromator (defined as the full width at half maximum (FWHM) of the spectrum) is limited by the resolving power of the gratings, the XUV source size and aberrations of the focusing optics. These effects put practical limits on the width of the slit used to filter the desired XUV wavelength. The experimental measurement of the spectral resolution employs XUV photoionization of helium and xenon atoms in the interaction region of the velocity map imaging spectrometer. The kinetic energy of the photoelectrons is equal to the difference between the XUV photon energy and the ionization potential (IP) of the target atom. Therefore, the width of the photoionization peak

detected in the VMI spectrometer is directly related to the bandwidth of the XUV light passing through the slit of the monochromator beamline. The VMI spectrometer additionally broadens the photoelectron peaks by about 2% of the kinetic energy of the electron. The target gas is chosen such as to minimize the kinetic energy of the photoelectrons and thus reduce the effect of the VMI energy resolution. For the high photon energies (harmonics 19 to 27) He atoms with an ionization potential (IP) of 24.59 eV are used. For lower harmonics (11th and 15th), which have an insufficient photon energy to ionize helium, we employ Xe atoms with an IP of 12.13 eV. The ground state of Xe ions has a spin-orbit splitting of 1.31 eV. This splitting is sufficiently large and can be fully resolved in the VMI spectra. Therefore it does not affect the monochromator resolution measurements.

In the experiments, first the bandwidth of the 19th harmonic is analyzed using the 300 grooves/mm gratings and four different slits with widths of 650, 200, 100 and 50 μm . Analysis of the photoelectron spectra shows that the bandwidth of the XUV light passing through the beamline is reduced when going from 650 μm to 200 μm slit and from 200 μm to 100 μm slit, but the bandwidth is practically identical for the 100 μm and 50 μm slits. We therefore conclude, that 100 μm is the practical limit for the slit width, at least for the case of the 19th harmonic. Next, for each grating pair two or three harmonics are selected from the XUV spectrum using the 100 μm slit and the width of the photoelectron peak is recorded in the VMI. For each combination of harmonic and grating, photoelectron spectra are also recorded without the slit to determine the input XUV bandwidth. It is important to ensure that the input bandwidth is substantially wider than the bandwidth selected by the 100 μm slit, since otherwise the spectral shape of the input radiation significantly influences the bandwidth of the output and invalidates the resolution measurement.

The results of the experimental series are presented in Fig. 8 as filled circles with colors corresponding to the three grating sets. The figure also includes estimates of the spectral resolution, which are calculated by ray-tracing of the optical layout with the assumptions that the XUV source size is equal to 60 μm and that the XUV beam divergence is 1 mrad independent of the harmonic order (estimated from the focusing conditions of the driving IR beam²⁸). The geometric aberrations, which limit spectral resolution by increasing the source image size at the position of the slit, are estimated at the alignment phase and amount to 90 μm (FWHM image size of an infinitely small source) independent of the XUV photon energy. Fig. 8 demonstrates that the results of these estimates are in very good agreement with the measurements, which serves as additional confirmation of the proper alignment of the monochromator beamline. The optimal spectral resolution of the monochromator is less than 500 meV for photon energies below 45 eV and increases to 600 meV at the limiting photon energy of 50 eV. The plot in Fig. 8 combined with the transmis-

sion data in Fig. 7 can serve as a guide for choosing the grating groove density and the slit width for the specific XUV photon energy.

Temporal characterization

The temporal characterization of the monochromator is performed using the process of sideband generation^{14,15}. In experiments of this kind, the atoms of a rare gas (in this case argon) are ionized by the XUV pulse in the presence of a moderately strong IR pulse. The electric field of the IR pulse modifies the kinetic energy of the photoelectrons resulting in additional features (sidebands) in the photoelectron kinetic energy distribution. The kinetic energies of the sidebands are shifted with respect to the main photoline by an integer number of IR photons, both to lower and higher energies.

Fig. 9 shows photoelectron VMI images recorded for ionization of Ar atoms by harmonic 23 (35.9 eV) without the IR field (left side) and in the presence of the IR pulse at zero time delay (right side). The image without the IR shows two distinct outer rings and three rings close to the center (at low kinetic energies). The outermost ring corresponds to photoionization producing the Ar^+ ($3s^2 3p^5 \ ^2P$) ionic final state. This state has a spin-orbit splitting of about 180 meV, which cannot be resolved in the present experiments. The second ring corresponds to the Ar^+ ($3s^1 3p^6 \ ^2S$) ionic state. The structures with low kinetic energies can be assigned to the formation of several electronically excited states of Ar^+ . In the right half of Fig. 9 the image is strongly modified by the presence of an IR pulse with an energy of 130 μJ . The main rings corresponding to single-photon ionization by the XUV pulse are weaker and many additional concentric rings (sidebands) appear with an energy spacing of the IR photon energy.

The temporal properties of both the XUV and IR pulses are investigated by scanning the time delay between the pulses. The variation of the intensity of the IR field at the time of the arrival of the XUV pulse is reflected in the intensities of the sidebands. For a sufficiently long IR pulse and high XUV photon energy the intensity of the n -th sideband for a fixed photoemission angle depends on the electric field of the IR pulse as follows^{14,15}:

$$S_n(\vec{k}) \propto J_n^2(x), x = \frac{\vec{E} \cdot \vec{k}}{\omega^2}, \quad (5)$$

where \vec{k} is the momentum of the electron, \vec{E} is the maximum electric field experienced by the electron, ω is the frequency of the IR field (all quantities are in atomic units) and $J_n(x)$ is the n -th order Bessel function. For sufficiently weak electric fields used in this experiment, the argument of the Bessel function is small and $J_n^2(x)$ is proportional to x^{2n} , i.e. to the IR pulse intensity.

The maximum electric field experienced by the photoelectron varies with time delay according to the envelope

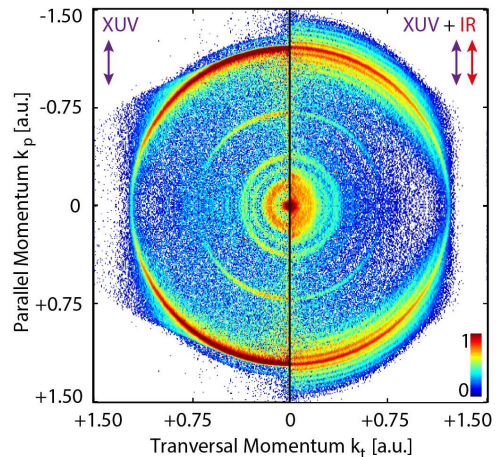


FIG. 9. Left: momentum map of photoelectrons produced by ionization of argon atoms by the 23rd harmonic (35.9 eV). The polarization of the XUV light is vertical. Right: similar momentum map in presence of the strong IR field. Sidebands appear as concentric rings in the vicinity of main photolines.

of the the electric field of the pulse. The temporal profile of the n -th sideband can be calculated as a convolution of the XUV pulse profile with the IR pulse intensity profile raised to the power of n . If both XUV and IR pulses have Gaussian shapes with a FWHM of Δt_{XUV} and Δt_{IR} , the temporal profile of the first and second sidebands are given by Gaussian distributions with widths:

$$\begin{aligned} \Delta t_1^2 &= \Delta t_{XUV}^2 + \Delta t_{IR}^2 \\ \Delta t_2^2 &= \Delta t_{XUV}^2 + \Delta t_{IR}^2/2. \end{aligned} \quad (6)$$

These expressions allow a calculation of both the XUV and IR pulse durations. Fig. 10a shows a false color map of the photoelectron kinetic energy distributions as a function of XUV-IR time delay measured with 300 gr/mm gratings and a 100 μm slit. The temporal profiles of the two positive sidebands (those shifted to higher energies with respect to the photoline) are plotted in Fig. 10c along with Gaussian fit functions. The extracted full widths at half maximum (FWHM) for the two sidebands are $\Delta t_1 = 38.8 \pm 0.4$ fs and $\Delta t_2 = 28.8 \pm 0.6$ fs. Using the expressions in Eq. 6 values of $\Delta t_{IR} = 37 \pm 1$ fs and $\Delta t_{XUV} = 12 \pm 3$ fs are extracted for the FWHM of the IR and XUV pulses, respectively. The width of the XUV pulse is remarkably close to the value of 13 ± 0.5 fs demonstrated previously using a similar time delay compensating monochromator²⁵. This measurement indicates, that our IR pulse is somewhat stretched due to slightly unequal amounts of dispersive material in the XUV and IR beam paths.

To quantify the compensation effect induced by the second stage of the TDCM, temporal profiles of the sidebands are measured with the second grating G2 positioned at zero angle (no compensation). The false color map of delay-dependent photoelectron kinetic energy distributions is shown in Fig. 10b. The temporal profile of

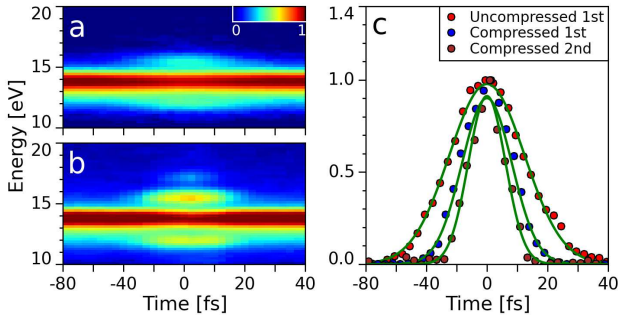


FIG. 10. Time- and energy- resolved sidebands generated in argon by the 19th harmonic (29.6 eV). The sideband intensity is integrated over all emission angles. a) Transient map for the fully compressed XUV beam. b) A similar map for the uncompressed XUV beam (the second grating is at zero order). c) Temporal profiles of the first and second positive sidebands of the compressed pulse and of the first positive sideband of the uncompressed pulse. The profiles are closely represented by Gaussian distributions with parameters described in the text.

the first order sideband is plotted in Fig. 10c and is visibly wider than the profiles obtained in the experiment with compensation. The measured FWHM of the sideband is 60 ± 1 fs, which results in a temporal duration of the stretched XUV pulse of 47 ± 1 fs, i.e. the XUV pulse is stretched by a factor of 3.1 upon diffraction off grating G1. This stretching corresponds to illumination of 340 grooves or a spot size of about 1.1 mm on the 300 grooves/mm grating used in the present experiments. This number is compatible with the XUV spot size of 0.8 mm roughly estimated from the divergence of the driving IR beam²⁸.

The results of temporal characterization demonstrate, that the monochromator preserves the XUV pulse duration within the accuracy of the current measurement (± 3 fs). According to the ray-tracing results presented above the theoretical limit for the current design is on the order of 2-4 fs depending on the XUV photon energy. This limit will be practically tested in future experiments, which will employ sub-10 fs IR pulses for generation and characterization of the temporal resolution.

V. APPLICATION TO SIDEBAND GENERATION IN IR-ASSISTED XUV IONIZATION OF ARGON ATOMS

The performance of the TDCM setup is demonstrated by investigating the process of sidebands generation in IR-assisted XUV ionization of argon atoms²⁶. In the previous section this process was used for temporal characterization employing relatively weak IR pulses, which results in only a few sideband orders. When the energy of the IR pulse is increased, many more sidebands can be observed. Fig. 11 shows photoelectron kinetic energy spectra for Ar atoms ionized by the 17th, 21st and 23rd

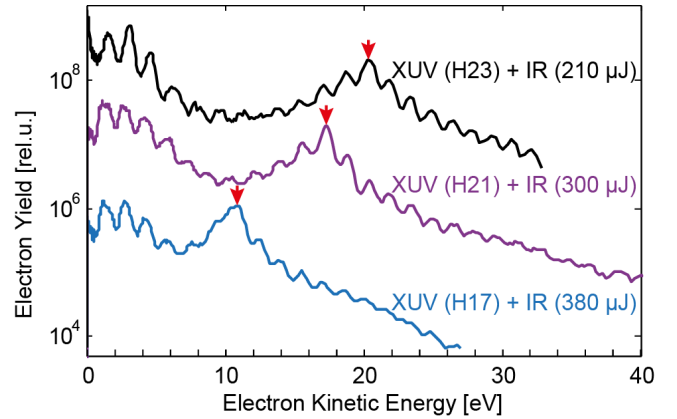


FIG. 11. Ionization of argon atoms by harmonics 17, 21 and 23 in the presence of a strong IR field (pulse energies are shown in the labels). The photoelectron distributions are integrated in the angular range of $\pm 15^\circ$ from the polarization axis. The positions of the main photoelectron distributions are marked by red arrows. The structures at low kinetic energies are attributed to above-threshold ionization of argon atoms by the IR pulses.

harmonics in the presence of an IR field. Up to 13 sidebands can be seen accompanying the main photoemission line corresponding to the $\text{Ar}^+ (3s^2 3p^5 \ ^2P)$ final state (labeled by an arrow), which shifts with the energy of the XUV photon.

The sideband intensity and their number depend on the electric field of the IR pulse at the moment of ionization by the XUV pulse^{14,15}. Therefore sideband measurements can be used to determine the IR laser pulse intensity at the focus, knowledge of which is essential for design and implementation of most pump-probe experiments. Electron kinetic energy distributions for several different IR pulse energies are shown in Fig. 12a. Only few sidebands are generated at the lowest pulse energy of 20 μJ . For higher pulse energies the number of sidebands substantially increases. Plotted on a logarithmic scale, the fall-off of the sideband intensity shows a characteristic piecewise linear behavior²⁹. The slope of the fall-off changes approximately at the positions indicated by arrows. These energies, called "cut-off" energies, are related to the maximum kinetic energy, which an electron created by the XUV pulse can classically acquire through interaction with the IR pulse. For positive and negative sidebands they are expressed (in atomic units) as^{15,29}:

$$E_{c\pm} = E_0 \pm \sqrt{8E_0U_p} + 2U_p, \quad (7)$$

where E_0 is the initial energy of the photoelectron given by the difference between the XUV photon energy and the ionization potential and

$$U_p[\text{eV}] = 9.338 \times 10^{-8} \times (\lambda_{IR}[\text{nm}])^2 \times I_{IR}[\text{TW}/\text{cm}^2]$$

is the ponderomotive potential of the IR field.

Thus the value of the cut-off energy can be used to calculate the average intensity of the IR field at the focus.

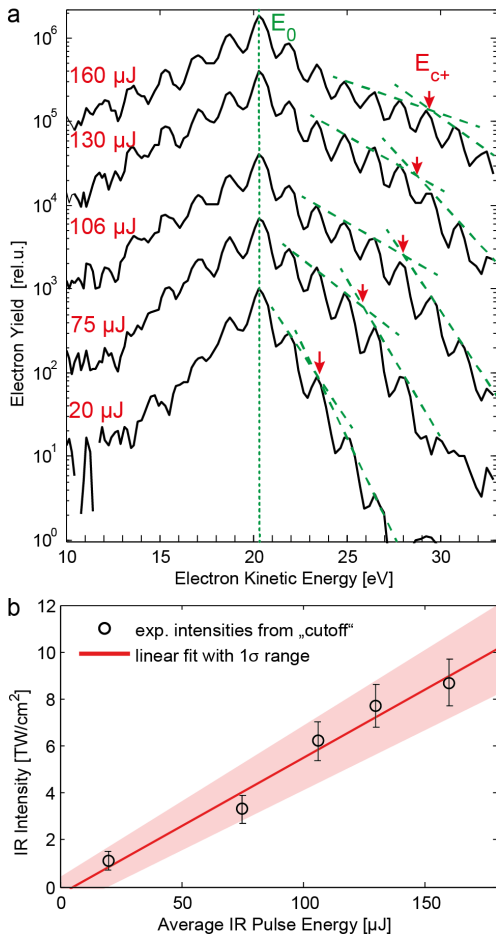


FIG. 12. Calibration of the intensity of the 800 nm IR pulse using a "cut-off" law for the sideband generation process. a) Sideband intensity distributions plotted on a logarithmic scale for five pulse energies from $20 \mu\text{J}$ to $160 \mu\text{J}$. The photoelectron distributions are integrated in the angular range of $\pm 10^\circ$ from the polarization axis. The spectra are shifted with respect to each other for better visibility. The positions of the "cut-off" energy E_{c+} for each curve are labelled with arrows. b) IR intensity derived from the "cut-off" energies for the five pulse energies. Linear regression provides the scaling of the IR intensity at the focus as a function of the pulse energy. The non-zero origin of the regression line is due to a systematic offset in the powermeter reading.

This method is more reliable than estimations based on the laser beam parameters such as pulse duration and size of the focal spot. Fig. 12b shows the field intensity calculations based on the "cut-off" law for five values of the pulse energy. As expected, the intensity is linearly proportional to the IR pulse energy. The coefficient of proportionality of $67 \pm 6 \text{ GW}/\text{cm}^2/\mu\text{J}$ gives an estimate of the beam FWHM at the focus of $140 \mu\text{m}^{26}$.

VI. CONCLUSIONS

In conclusion, we have implemented a time delay compensating XUV monochromator suitable for femtosecond pump-probe experiments with wavelength-selected XUV pulses. The beamline is designed to operate in the photon energy range from 3 to 50 eV. The XUV radiation is produced by means of high-order harmonic generation, which is demonstrated to deliver XUV pulses with durations of 12 ± 3 fs for the harmonic 19. This duration is compatible with the expected duration of the XUV pulse generated at the present experimental conditions and is preserved by the monochromator beamline thanks to the two-grating design. The transmission of the beamline varies from 3% to 15% depending on the photon energy. The optimal spectral resolution of the beamline varies from 300 meV to 500 meV FWHM for the photon energies below 45 eV and increases to 600 meV at the limiting photon energy of 50 eV.

We analyze the most sensitive parameters for TDCM alignment, present the ray-tracing calculations and practical implementation of the alignment procedure, which ensures stable and reliable operation of the TDCM beamline in long experimental measurements and enables flawless switching between XUV photon energies in the course of experiments. The demonstrated alignment strategy can be applied in implementations of other XUV optical schemes, which use conical diffraction.

The TDCM beamline in combination with a velocity map imaging spectrometer is used to investigate generation of IR-assisted sidebands in the XUV photoionization of argon atoms. The atoms are ionized by XUV pulses in presence of IR pulses with variable pulse energy. The number of observed sidebands and their intensity depend on the strength of the electric field, which is used to determine the intensity of the IR pulses at the focus.

The implementation of TDCM presented here demonstrates specifications, which are very close to theoretical expectations. The transmission in the current design is limited by the coatings of the optical elements and the choice of blaze angles for the gratings. The setup can thus be optimized for specific wavelength ranges by installing gratings with the optimal blaze angle without any further modifications. The spectral resolution of the setup is mostly limited by geometric aberrations in imaging by toroidal mirrors. If required, it can be improved by replacing the toroidal mirrors with parabolic mirrors, which however will require a very precise alignment³⁰. The use of parabolic mirrors can also improve the temporal resolution of the TDCM and open a way to implementation of wavelength selected attosecond XUV pulses.

ACKNOWLEDGMENTS

We would like to thank Roman Peslin, Reinhard Grosser, Arje Katz, Thomas Müller, Kathrin Lange and Geert Reitsma for their help in design, construction and

characterization of the monochromator beamline.

- ¹F. Calegari, D. Ayuso, A. Trabattoni, L. Belshaw, S. De Camillis, S. Anumula, F. Frassetto, L. Poletto, A. Palacios, P. Decleva, J. B. Greenwood, F. Martn, and M. Nisoli, *Science* **346**, 336 (2014).
- ²M. Eckstein, C.-H. Yang, M. Kubin, F. Frassetto, L. Poletto, H.-H. Ritze, M. J. J. Vrakking, and O. Kornilov, *J. Phys. Chem. Lett.* **6**, 419 (2015).
- ³P. Siffalovic, M. Drescher, M. Spieweck, T. Wiesenthal, Y. C. Lim, R. Weidner, A. Elizarov, and U. Heinzmann, *Rev. Sci. Instrum.* **72**, 30 (2001).
- ⁴L. Nugent-Glandorf, M. Scheer, D. A. Samuels, V. Bierbaum, and S. R. Leone, *Rev. Sci. Instrum.* **73**, 1875 (2002).
- ⁵M. Ito, Y. Kataoka, T. Okamoto, M. Yamashita, and T. Sekikawa, *Opt. Express* **18**, 6071 (2010).
- ⁶L. Poletto, P. Villoresi, E. Benedetti, F. Ferrari, S. Stagira, G. Sansone, and M. Nisoli, *Opt. Lett.* **32**, 2897 (2007).
- ⁷G. L. Dakovski, Y. Li, T. Durakiewicz, and G. Rodriguez, *Rev. Sci. Instrum.* **81**, 073108 (2010).
- ⁸B. Frietsch, R. Carley, K. Dbrich, C. Gahl, M. Teichmann, O. Schwarzkopf, P. Wernet, and M. Weinelt, *Rev. Sci. Instrum.* **84**, 075106 (2013).
- ⁹J. Gaudin, S. Rehbein, P. Guttmann, S. God, G. Schneider, P. Wernet, and W. Eberhardt, *J. Appl. Phys.* **104**, 033112 (2008).
- ¹⁰M. Ibek, T. Leitner, A. Erko, A. Firsov, and P. Wernet, *Rev. Sci. Instrum.* **84**, 103102 (2013).
- ¹¹J. Metje, M. Borgwardt, A. Moguilevski, A. Kothe, N. Engel, M. Wilke, R. Al-Obaidi, D. Tolksdorf, A. Firsov, M. Brzhezinskaya, A. Erko, I. Y. Kiyani, and E. F. Aziz, *Opt. Express* **22**, 10747 (2014).
- ¹²P. Villoresi, *Appl. Opt.* **38**, 6040 (1999).
- ¹³L. Poletto, *Appl. Phys. B: Lasers Opt.* **78**, 1013 (2004).
- ¹⁴N. M. Kroll and K. M. Watson, *Phys. Rev. A* **8**, 804 (1973).
- ¹⁵A. Maquet and R. Taieb, *J. Mod. Opt.* **54**, 1847 (2007).
- ¹⁶W. Werner, *Appl. Opt.* **16**, 2078 (1977).
- ¹⁷M. Neviere, P. Vincent, and D. Maystre, *Appl. Opt.* **17**, 843 (1978).
- ¹⁸L. Poletto and P. Villoresi, *Appl. Opt.* **45**, 8577 (2006).
- ¹⁹M. Pascolini, S. Bonora, A. Giglia, N. Mahne, S. Nannarone, and L. Poletto, *Appl. Opt.* **45**, 3253 (2006).
- ²⁰T. Pfeifer, C. Spielmann, and G. Gerber, *Rep. Prog. Phys.* **69**, 443 (2006).
- ²¹O. Kornilov, R. Wilcox, and O. Gessner, *Rev. Sci. Instrum.* **81**, 063109 (2010).
- ²²A. T. J. B. Eppink and D. H. Parker, *Rev. Sci. Instrum.* **68**, 3477 (1997).
- ²³O. Ghafur, W. Siu, P. Johnsson, M. F. Kling, M. Drescher, and M. J. J. Vrakking, *Rev. Sci. Instrum.* **80**, 033110 (2009).
- ²⁴P. Johnsson, A. Rouzée, W. Siu, Y. Huisman, F. Lépine, T. Marchenko, S. Düsterer, F. Tavella, N. Stojanovic, H. Redlin, A. Azima, and M. J. J. Vrakking, *Opt. Lett.* **35**, 4163 (2010).
- ²⁵L. Poletto, P. Villoresi, F. Frassetto, F. Calegari, F. Ferrari, M. Lucchini, G. Sansone, and M. Nisoli, *Rev. Sci. Instrum.* **80**, 123109 (2009).
- ²⁶M. Kubin, *Wavelength-Tunable XUV-Pulses for Femtosecond XUV-IR Nonlinear Effects*, Master's thesis, Freie Universitt Berlin (2013).
- ²⁷The transmission measurement for the photon energy range of the 150 gr/mm grating could not be carried out because the Al filter, which is required to protect the photodiodes from the residual IR light, has very low transmission in the energy range of this grating. This poses no problems for using the grating in experiments, which are not sensitive to a stray IR light.
- ²⁸P. Salieres, T. Ditmire, M. D. Perry, A. L'Huillier, and M. Lewenstein, *J. Phys. B: At., Mol. Opt. Phys.* **29**, 4771 (1996).
- ²⁹P. Radcliffe, M. Arbeiter, W. B. Li, S. Düsterer, H. Redlin, P. Hayden, P. Hough, V. Richardson, J. T. Costello, T. Fennel, and M. Meyer, *New J. of Phys.* **14**, 043008 (2012).
- ³⁰F. Frassetto, P. Villoresi, and L. Poletto, *Opt. Express* **16**, 6652 (2008).